

Article

Rb₂Na(NO₃)₃: A Congruently Melting UV-NLO Crystal with a Very Strong Second-Harmonic Generation Response

Guohong Zou ¹, Chensheng Lin ², Hyung Gu Kim ¹, Hongil Jo ¹ and Kang Min Ok ^{1,*}

¹ Department of Chemistry, Chung-Ang University, Seoul 06974, Korea; zough@caep.cn (G.Z.); cosmose0@naver.com (H.G.K.); hongil55@hanmail.net (H.J.)

² Fujian Institute of Research on the Structure of Matter, Chinese Academy of Sciences, Fuzhou 350002, China; cslin@fjirsm.ac.cn

* Correspondence: kmok@cau.ac.kr; Tel.: +82-2-820-5197; Fax: +82-2-825-4736

Academic Editors: Ning Ye and Helmut Coelfen

Received: 26 January 2016; Accepted: 7 April 2016; Published: 13 April 2016

Abstract: Crystals of congruently melting noncentrosymmetric (NCS) mixed alkali metal nitrate, Rb₂Na(NO₃)₃, have been grown through solid state reactions. The material possesses layers with NaO₈ hexagonal bipyramids and NO₃ triangular units. Rb⁺ cations are residing in the interlayer space. Each NaO₈ hexagonal bipyramid shares its corners and edges with two and three NO₃ units, respectively, in order to fulfill a highly dense stacking in the unit cell. The NaO₈ groups share their six oxygen atoms in equatorial positions with three different NO₃ groups to generate a NaO₆-NO₃ layer with a parallel alignment. The optimized arrangement of the NO₃ groups and their high density in the structure together produce a strong second-harmonic generation (SHG) response. Powder SHG measurements indicate that Rb₂Na(NO₃)₃ has a strong SHG efficiency of five times that of KH₂PO₄ (KDP) and is type I phase-matchable. The calculated average nonlinear optical (NLO) susceptibility of Rb₂Na(NO₃)₃ turns out to be the largest value among the NLO materials composed of only [NO₃][−] anion. In addition, Rb₂Na(NO₃)₃ exhibits a wide transparency region ranging from UV to near IR, which suggests that the compound is a promising NLO material.

Keywords: nonlinear optical materials; alkali metal nitrate; UV; theory calculation; strong SHG responses

1. Introduction

Nonlinear optical (NLO) crystals, especially those producing coherent ultraviolet (UV) light, are continuously attracting enormous attention, attributed to their auspicious applications in laser science and technology [1–14]. To be a useful UV-NLO material, however, it should exhibit a high NLO coefficient and a wide UV transmittance. Recently, many borate-based UV-NLO crystals [15–22] revealing a variety of structural possibilities and considerably large microscopic second-order susceptibility with moderate birefringence based on the anionic group theory have been reported [23–25]. A few representative materials include β-BaB₂O₄ (BBO) [16], LiB₃O₅ (LBO) [17], CsB₃O₅ (CBO) [18], CsLiB₆O₁₀ (CLBO) [19,20], KBe₂BO₃F₂ (KBBF) [21], and Sr₂Be₂B₂O₇ (SBBO) [22]. The unique advantage of the [BO₃]^{3−} group has motivated many chemists' interests further in finding new NLO materials with other functional groups, such as nitrates and carbonates. Specifically, [NO₃][−] and [CO₃]^{2−} groups possess the similar π-conjugated molecular orbitals in trigonal planar structures. Recently, materials containing carbonates have been widely studied, and a series of relevant materials exhibiting excellent NLO characteristics have been uncovered [26–33]. Systematic examinations of [NO₃][−]-containing materials with proper NLO properties, however, have rarely been achieved in

contrast to the successful investigations of carbonates and borates [34–37]. In fact, there is no known nitrate compound that can be used as a practical NLO material up to now. On the basis of Li's calculations, the microscopic second-order susceptibility, $\beta^{(2)}$, of the $[\text{NO}_3]^-$ group is expected to be larger than that of the $[\text{BO}_3]^{3-}$ or $[\text{CO}_3]^{2-}$ group [38]. Therefore, we have chosen the $[\text{NO}_3]^-$ anionic group as a basic building unit to develop novel UV-NLO crystals with high NLO coefficients. In order to obtain NLO materials exhibiting strong second-harmonic generation (SHG) effects, a number of methods have been discussed. Combining asymmetric building units, such as distorted octahedra with a d^0 transition metal cation [39–41], polyhedra with a d^{10} metal cation revealing a polar displacement [42,43], and metal ions with ns^2 lone pair electrons [44] in the frameworks of new materials is a common approach to increase the incidence of many good NLO materials [45,46]. Incorporation of the above mentioned acentric building units into a nitrates system may also enlarge the SHG efficiency of materials. However, a critical issue found from all these design strategies is that the absorption edge is red-shifted with the building blocks. To warrant high transmission in the UV region, counter cations that do not exhibit $d-d$ or $f-f$ transitions, such as alkali metals and alkaline earth metals, should be incorporated. Based on the relationships between the structures and overall NLO properties, there are two approaches to produce large NLO effects: (i) choosing favorable structural units and having them aligned in a parallel manner, and (ii) increasing the density of the NLO structural units. In this article, we report phase pure synthesis, structure determination, characterization, and calculations of a promising UV-NLO material, $\text{Rb}_2\text{Na}(\text{NO}_3)_3$. To the best of our knowledge, the reported material reveals the largest average NLO susceptibility among the NLO materials containing only $[\text{NO}_3]^-$ anion.

2. Results and Discussion

2.1. Crystal Structure Description

The structure of $\text{Rb}_2\text{Na}(\text{NO}_3)_3$ has been recently reported using a crystal obtained from the study of the NaNO_3 – RbNO_3 phase diagram [47]. However, we redetermined the crystal structure of the material in order to better understand the details of the NLO properties. In this study, high quality single crystals of $\text{Rb}_2\text{Na}(\text{NO}_3)_3$ have been easily grown using NH_4NO_3 as flux. $\text{Rb}_2\text{Na}(\text{NO}_3)_3$ crystallizes in an orthorhombic polar noncentrosymmetric (NCS) space group, $Pmc2_1$ (No. 26). $\text{Rb}_2\text{Na}(\text{NO}_3)_3$ exhibits a layered structure that consists of NaO_8 hexagonal bipyramids and NO_3 trigonal plane units. Rb^+ cations reside in the interlayer space and make an overall charge balance. Within the layer, the N is coordinated to three O atoms to generate an NO_3 trigonal plane unit with the N–O bond lengths of 1.228(3)–1.265(4) Å and O–N–O bond angles of 117.6(2)–124.7(4)°. The Na is coordinated to six equatorial O atoms and two apical O atoms to create NaO_8 hexagonal bipyramids (see Figure 1a). The Na–O bond lengths in the NaO_8 polyhedra range from 2.332(3) to 2.685(3) Å. Each NaO_8 hexagonal bipyramid shares its corners through oxygen atoms and forms a 1D chain structure along the a -direction (see Figure 1b). Then the 1D chains are further connected by NO_3 groups and a layer parallel to the bc -plane is obtained (see Figure 1c). As seen in Figure 1c,d, NO_3 groups serve as both intra- and inter-chain linkers. In connectivity terms, the material may be described as an anionic layer of $\{[\text{Na}(1)\text{O}_{6/2}\text{O}_{2/3}]^{6.333-} \cdot [\text{N}(1)\text{O}_{1/2}\text{O}_{2/1}]^0 \cdot [\text{N}(2)\text{O}_{1/3}\text{O}_{2/2}]^{2.333+} \cdot [\text{N}(3)\text{O}_{3/2}]^{2+}\}^{2-}$, with the charge balance maintained by two Rb^+ cations. Each NaO_8 hexagonal bipyramid shares its corners and edges with two and three NO_3 triangles, respectively. While the oxygen atoms in $\text{N}(2)\text{O}_3$ and $\text{N}(3)\text{O}_3$ groups are connected to Na, the two oxygen atoms in $\text{N}(1)\text{O}_3$ are not linked further and are dangling. The NaO_8 polyhedra share their six equatorial oxygen atoms with three separate NO_3 groups to generate a flat NaO_6 – NO_3 layer. Owing to its special coordination, the NaO_6 moiety in the flat layer pushes its three adjacent NO_3 groups to array into a perfect parallel alignment and result in maximum contribution to the SHG effect. The other two NO_3 groups are inclined to the NaO_6 – NO_3 layer, giving additional contributions to the SHG effect.

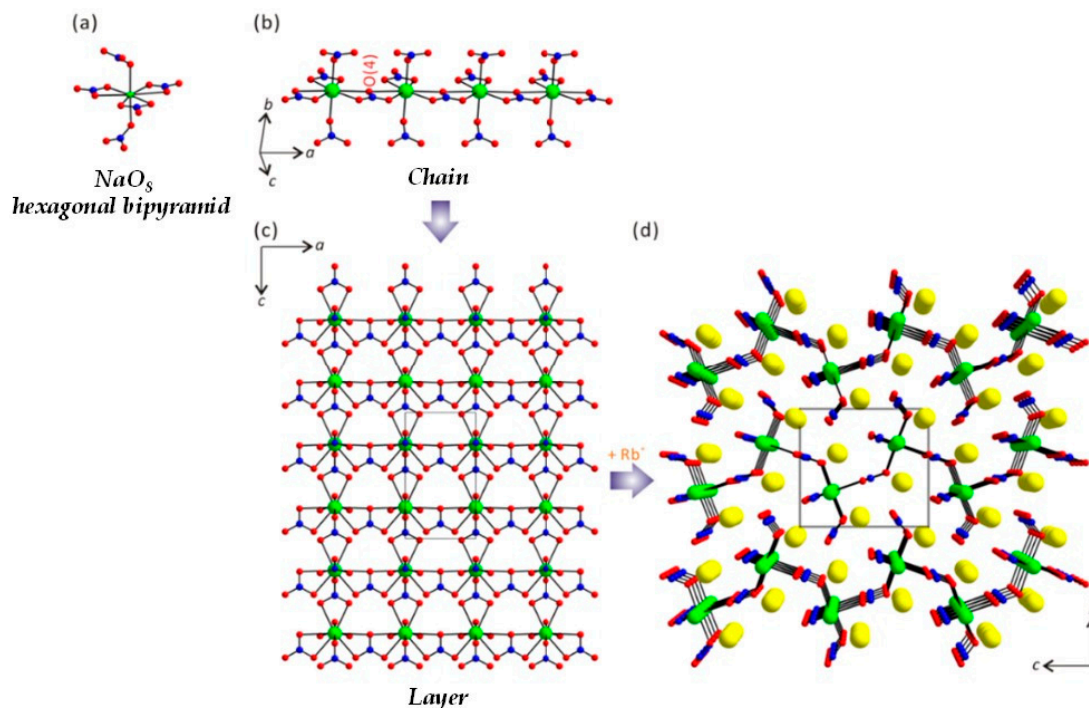


Figure 1. Ball-and-stick model representing (a) the NaO_8 hexagonal bipyramid; (b) 1D chain along the a -axis; (c) one layer in the ac -plane; and (d) a complete layered structure in the bc -plane for $\text{Rb}_2\text{Na}(\text{NO}_3)_3$ (green, Na; blue, N; yellow, Rb; red, O). Note the NO_3 groups serve as intra- and inter-chain linkers.

The bond valence sums for $\text{Rb}_2\text{Na}(\text{NO}_3)_3$ are calculated using the following formula

$$V_i = \sum_j S_{ij} = \sum_j \exp \left\{ \frac{r_0 - r_{ij}}{B} \right\}$$

where S_{ij} is the bond valence associated with bond length, and r_{ij} , r_0 , and B (usually 0.37) are empirically determined parameters [48,49]. The calculated bond valences for Rb^+ , Na^+ , N^{5+} , and O^{2-} atoms in $\text{Rb}_2\text{Na}(\text{NO}_3)_3$ are 1.14–1.22, 1.13, 4.94–5.04, and 1.97–2.13, respectively.

2.2. Thermal Properties

The thermal behavior of $\text{Rb}_2\text{Na}(\text{NO}_3)_3$ was investigated using thermogravimetric/differential thermal analysis (TG/DTA). As seen in Figure 2a, the DTA curve for $\text{Rb}_2\text{Na}(\text{NO}_3)_3$ exhibits only one endothermic peak at 182 °C, along with a negligible weight loss observed in the TGA curve, possibly due to the volatility upon melting. In addition, analysis of the powder XRD patterns for $\text{Rb}_2\text{Na}(\text{NO}_3)_3$ before and after melting strongly suggests that $\text{Rb}_2\text{Na}(\text{NO}_3)_3$ does not change the phase all the time, and melts congruently (see Figure 2b). Therefore, we believe that large crystals of $\text{Rb}_2\text{Na}(\text{NO}_3)_3$ could be easily grown in air.

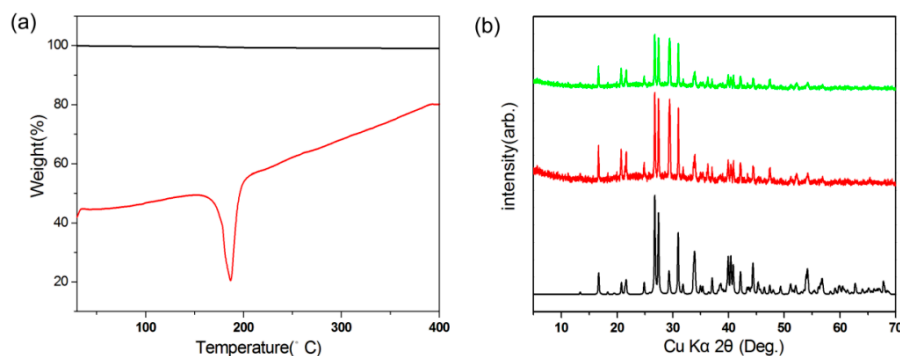


Figure 2. (a) Thermogravimetric/differential thermal analysis (TG/DTA) diagrams and (b) experimental and calculated powder X-ray diffraction (PXRD) patterns for $\text{Rb}_2\text{Na}(\text{NO}_3)_3$. Only one endothermic peak in the DTA curve and the identical PXRD patterns before and after melting suggest that $\text{Rb}_2\text{Na}(\text{NO}_3)_3$ does not change the phase all the time and melts congruently.

2.3. Optical Properties

UV-vis diffuse reflectance spectral data for $\text{Rb}_2\text{Na}(\text{NO}_3)_3$ were collected (see Figure 3a). Absorption data (K/S) were worked out from the following Kubelka–Munk function [50,51]:

$$F(R) = \frac{(1 - R)^2}{2R} = \frac{K}{S}$$

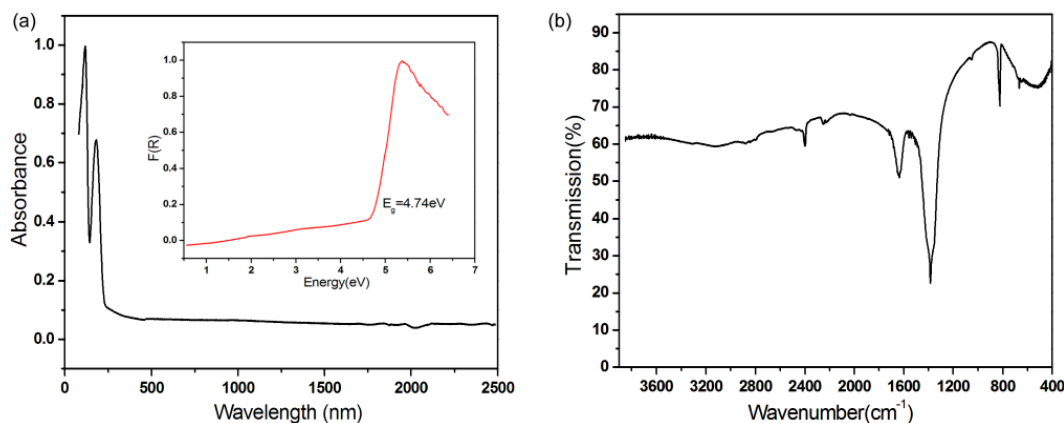


Figure 3. (a) UV-vis and (b) IR spectra of $\text{Rb}_2\text{Na}(\text{NO}_3)_3$.

In which K is the absorption, R is the reflectance, and S is the scattering. Extrapolating the linear part of the sloping upward curve to zero in the (K/S)-versus- E plot yields the appearance of absorption. No absorption from 0.27 to 2.5 μm in the UV-Vis-IR of $\text{Rb}_2\text{Na}(\text{NO}_3)_3$ indicates that the compound has wide transparent regions that range from near-UV to mid-IR. The optical band gap of $\text{Rb}_2\text{Na}(\text{NO}_3)_3$ is 4.74 eV. The relatively smaller optical band gap may be attributed to the two dangling oxygen atoms in $\text{N}(1)\text{O}_3$. It has been shown in borates that the terminal oxygen atoms red-shift the absorption edge, making it difficult to reach the deep-UV.

As seen in Figure 3b, the IR spectrum of $\text{Rb}_2\text{Na}(\text{NO}_3)_3$ reveals peaks at 1384 and 840 cm^{-1} , which can be assigned to the stretching and bending vibrations of $[\text{NO}_3]^-$ groups, respectively. Bands occurring at 1018 and 690 cm^{-1} are attributed to the asymmetric and symmetric stretches of $[\text{NO}_3]^-$ groups. The assignments are consistent with previously reported data [34–37].

2.4. NLO Properties

The curve of the SHG signal *vs.* particle size acquired from the measurements made on ground crystals of $\text{Rb}_2\text{Na}(\text{NO}_3)_3$ is shown in Figure 4a. The result is consistent with a type I phase-matching behavior according to the rule proposed by Kurtz and Perry [52]. $\text{Rb}_2\text{Na}(\text{NO}_3)_3$ exhibited a very large SHG response which was five times that of KH_2PO_4 (KDP) (see Figure 4b). Because the reported d_{36} coefficient for KDP is 0.39 pm/V [53], the derived d_{eff} coefficients for $\text{Rb}_2\text{Na}(\text{NO}_3)_3$ is 1.9 pm/V. It should be noted that the intensity is the largest reported to date among the NLO materials consisting of only $[\text{NO}_3]^-$ anion.

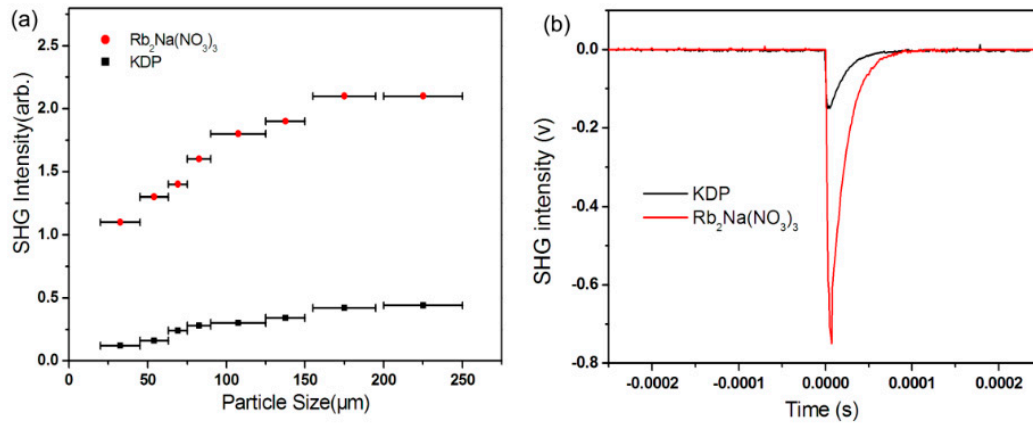


Figure 4. (a) Second-harmonic generation (SHG) intensity *vs.* particle size curves for $\text{Rb}_2\text{Na}(\text{NO}_3)_3$ and KH_2PO_4 (KDP) on a 1064 nm Q-switched Nd:YAG laser and (b) oscilloscope traces of the SHG signals for the powders (150–200 μm) of $\text{Rb}_2\text{Na}(\text{NO}_3)_3$ and KDP.

The dipole transition from the cations (Rb^+ and Na^+ in this case) to the anionic groups ($[\text{NO}_3]^-$ in this case) is the off-site transition, according to the anionic group theory [22–24]. Its value is about one order smaller than the dipole transition of the intra-atomic transitions within anionic groups. Therefore, the main contribution to the SHG coefficients in $\text{Rb}_2\text{Na}(\text{NO}_3)_3$ is from the anionic $[\text{NO}_3]^-$ groups. In other words, the transition within nitrate anions is much larger than that of the charge transfer between the *p*-originated states of anions and the *s*-states of cations. Therefore, the macroscopic second-order susceptibility $\chi^{(2)}$ could be demonstrated by Equation (1) based on the anionic group theory,

$$\chi_{ijk}^{(2)} = \frac{F}{V} \sum_P \sum_{i'j'k'} \alpha_{ii'} \alpha_{jj'} \alpha_{kk'} \beta_{i'j'k'}^{(2)}(P) P = [\text{NO}_3]^- \quad (1)$$

where F is the correction factor of the local field, V is the volume of the unit cell, $\alpha_{ii'}$, $\alpha_{jj'}$, and $\alpha_{kk'}$ are the direction cosines between the macroscopic coordinates of the crystal and the microscopic coordinates of $[\text{NO}_3]^-$ groups, and $\beta_{i'j'k'}^{(2)}$ is the microscopic second-order susceptibility tensors of an individual group. Owing to the fact that $[\text{NO}_3]^-$ is a planar group in point group D_{3h} , there are only two non-vanishing second-order susceptibilities, $\beta_{111}^{(2)} = \beta_{222}^{(2)}$. Since the geometrical factor, g , can be extracted from Equation (1),

$$\chi_{ijk}^{(2)} = \frac{F}{V} g_{ijk} \beta_{111}^{(2)}([\text{NO}_3]) \quad (2)$$

In the case of unspontaneous polarization, the structural criterion C is defined as:

$$C = \frac{g}{n} \quad (3)$$

Equation (2) may be simplified according to the deduction process shown in reference [54]:

$$\chi_{ijk}^{(2)} = F \times \left(\frac{n}{V}\right) \times C \times \beta_{111}([\text{NO}_3]) \quad (4)$$

where n is the number of anionic groups in a unit cell. Therefore, the NLO coefficient $\chi_{ijk}^{(2)}$ is proportional to the structural criterion (C) and the density of the $[\text{NO}_3]^-$ group (n/V). In the crystal structure of $\text{Rb}_2\text{Na}(\text{NO}_3)_3$, each NaO_8 trigonal bipyramid connects with five NO_3 groups (see Figure 1a). One NaO_8 polyhedron shares its six equatorial oxygen atoms with three of the five separate NO_3 groups to form a flat $\text{NaO}_6\text{-NO}_3$ layer. The three neighboring NO_3 groups put in order into a perfect parallel alignment to provide a major contribution to the C factor. The other two NO_3 groups are inclined to the $\text{NaO}_6\text{-NO}_3$ layer, giving additional contributions to the C factor. Following the computing method used previously [27,29], the calculated C factor for $\text{Rb}_2\text{Na}(\text{NO}_3)_3$ is to be 82%.

To obtain further understanding of the SHG effects as directed by the density of NLO-active groups and the arrangement of the NLO-active groups, the calculated coefficient of NLO effect for $\text{Rb}_2\text{Na}(\text{NO}_3)_3$ was compared with those for other nitrates NLO materials (see Table 1). Although the density of $[\text{NO}_3]^-$ and the structural criterion C for $\text{Rb}_2\text{Na}(\text{NO}_3)_3$ are not the largest in these six NCS nitrates, the SHG coefficient of $\text{Rb}_2\text{Na}(\text{NO}_3)_3$ is the largest. Although the structural criterion C for $\text{Rb}_2\text{Na}(\text{NO}_3)_3$ is lower than that of $\text{Sr}_2(\text{OH})_3\text{NO}_3$ (100%) [37], the SHG coefficient of $\text{Rb}_2\text{Na}(\text{NO}_3)_3$ is larger than that of $\text{Sr}_2(\text{OH})_3\text{NO}_3$. On the other hand, $\text{Rb}_2\text{Na}(\text{NO}_3)_3$ has a much higher density of $[\text{NO}_3]^-$ groups compared to $\text{Sr}_2(\text{OH})_3\text{NO}_3$. Though $\text{K}_2\text{La}(\text{NO}_3)_5 \cdot 2\text{H}_2\text{O}$ has the highest density of $[\text{NO}_3]^-$ groups, a small structural criterion C arising from its unfavorable arrangement of the $[\text{NO}_3]^-$ groups in the structure lead to a moderate SHG coefficient (see Figure S1). Thus, balancing the density of NLO-active groups and the structural criterion C is very important to the SHG coefficient. A relatively high density of $[\text{NO}_3]^-$ groups and a relatively large structural criterion values of C factors produce the strong NLO effect of $\text{Rb}_2\text{Na}(\text{NO}_3)_3$.

Table 1. Nonlinear optical (NLO) effects of $\text{Rb}_2\text{Na}(\text{NO}_3)_3$, $[\text{Pb}_4(\text{OH})_4](\text{NO}_3)_4$ [35], $[\text{LaPb}_8\text{O}(\text{OH})_{10}(\text{H}_2\text{O})](\text{NO}_3)_7$ [36], $\text{LaPb}_8\text{O}(\text{OH})_{10}(\text{H}_2\text{O})](\text{NO}_3)_7 \cdot 2\text{H}_2\text{O}$ [36], $\text{Sr}_2(\text{OH})_3\text{NO}_3$ [37], and $\text{K}_2\text{La}(\text{NO}_3)_5 \cdot 2\text{H}_2\text{O}$ [55].

Crystals	SHG Coefficient (Visible) (\times KDP)	Structural Criterion C	Density of $[\text{NO}_3]$ (n/V) (\AA^{-3})	$(n/V) \times C$ (\AA^{-3})
$\text{Rb}_2\text{Na}(\text{NO}_3)_3$	5	0.82	0.0128	0.0105
$[\text{Pb}_4(\text{OH})_4](\text{NO}_3)_4$	0.7	0.17	0.0109	0.0018
$[\text{LaPb}_8\text{O}(\text{OH})_{10}(\text{H}_2\text{O})](\text{NO}_3)_7$	1.3	0.32	0.0087	0.0028
$[\text{LaPb}_8\text{O}(\text{OH})_{10}(\text{H}_2\text{O})](\text{NO}_3)_7 \cdot 2\text{H}_2\text{O}$	1.1	0.31	0.0081	0.0025
$\text{Sr}_2(\text{OH})_3\text{NO}_3$	3.6	1.00	0.0075	0.0075
$\text{K}_2\text{La}(\text{NO}_3)_5 \cdot 2\text{H}_2\text{O}$	2.4	0.36	0.0135	0.0049

2.5. Theoretical Calculations

Band structure calculations reveal that $\text{Rb}_2\text{Na}(\text{NO}_3)_3$ has an indirect band gap of 3.24 eV (see Figure S2), which is smaller than the experimental value of 4.74 eV. The tendency for electronic band structure calculations with the DFT method to underestimate the band gap has been well documented [56–58]. Thus, the scissor value of 1.5 eV for $\text{Rb}_2\text{Na}(\text{NO}_3)_3$ is applied to the subsequent SHG calculations based on the Perdew–Burke–Ernzerhof (PBE) functional.

The total and partial densities of states (DOS and PDOS) for $\text{Rb}_2\text{Na}(\text{NO}_3)_3$ are presented in Figure 5. The valence bands (VB) spanning over -30.0 to -15.0 eV originate predominately from Rb 5s, Na 2p, O 2s, N 2s, and N 2p states as well as, to a lesser extent, from O 2p and Rb 4p states. VBs ranging from -10.0 to -5.0 eV are mostly formed by Rb 4p, N 2p, O 2p, and O 2s states hybridized with small amounts of Na 2p and N 2s states. VBs from -5.0 eV to the Fermi level (EF) are mostly from the contributions of O 2p states. O 2p and N 2p states make up the conduction bands (CB) between EF and 5.0 eV. CBs ranging from 5.0 to 10.0 eV mainly consist of Rb 5s and Rb 4p states with a small

portion of Na 2p, O 2p, and N 2s states. Because linear and nonlinear optical properties are mainly determined by the states close to the forbidden band that largely consists of the p orbital of the $[\text{NO}_3]^-$ groups, the electron transition is provided by inside excitation of the $[\text{NO}_3]^-$ group, indicating a great contribution from the NO_3 polyhedra to the SHG coefficients.

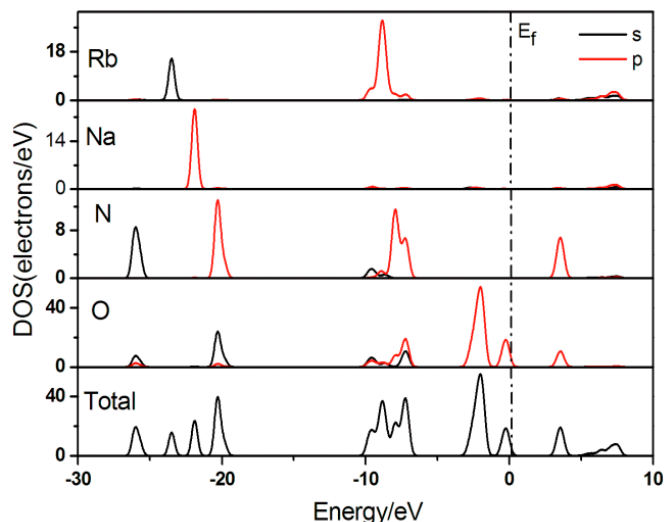


Figure 5. Total and partial densities of states (DOS/PDOS) for $\text{Rb}_2\text{Na}(\text{NO}_3)_3$.

Considering the spatial symmetry and the Kleinman's full permutation symmetry condition for a lossless nonlinear medium, crystal class with $mm2$ point group has only three independent nonvanishing elements, *i.e.*, d_{31} ($=d_{15}$), d_{32} ($=d_{24}$), and d_{33} . The calculated nonlinear coefficients are shown in Figure 6. At the pumping wavelength of 1064 nm, the calculated d_{ij} (Einstein shortened notation of the NLO coefficient $\chi_{ijk}^{(2)}$) coefficient values of PBE are as follows: $d_{15} = d_{31} = 3.48$ pm/V, $d_{24} = d_{32} = 0.83$ pm/V, and $d_{33} = 2.64$ pm/V. The discrepancy between calculated and experimental d_{ij} coefficient may arise from both the theoretical method and the experimental measurement. At the theoretical side, it's found that conventional density functional method like B3LYP overestimations of $\chi^{(1)}$ [59], which straightforward overestimate the $\chi^{(2)}$ according to Equation (6). Although we have applied the scissor-operation to modify the underestimated band gap given by the PBE exchange-correlation functional, it may still overestimate $\chi^{(1)}$. We also try the hybrid functional HSE06 and obtain the d_{ij} components: $d_{31} = 1.85$ pm/V, $d_{32} = 0.88$ pm/V, and $d_{33} = 1.35$ pm/V. It is a great improvement compared to the PBE functional, but is somewhat over-rectified. Furthermore, the anharmonic oscillator (AHO) model uses the atomic resonance frequency to estimate the local field factor, which could not offer the accurate in-crystal polarizing field effect. At the experiment side, our measurement is performed on powder samples while the theoretical models are built on the hypothesis of a perfect single crystal. Higher level theoretical methods, like explicitly calculating the d_{ij} by using electron correlation [60] and more accurate determination of the nonlinear coefficient on a single crystal will be the focus of future research.

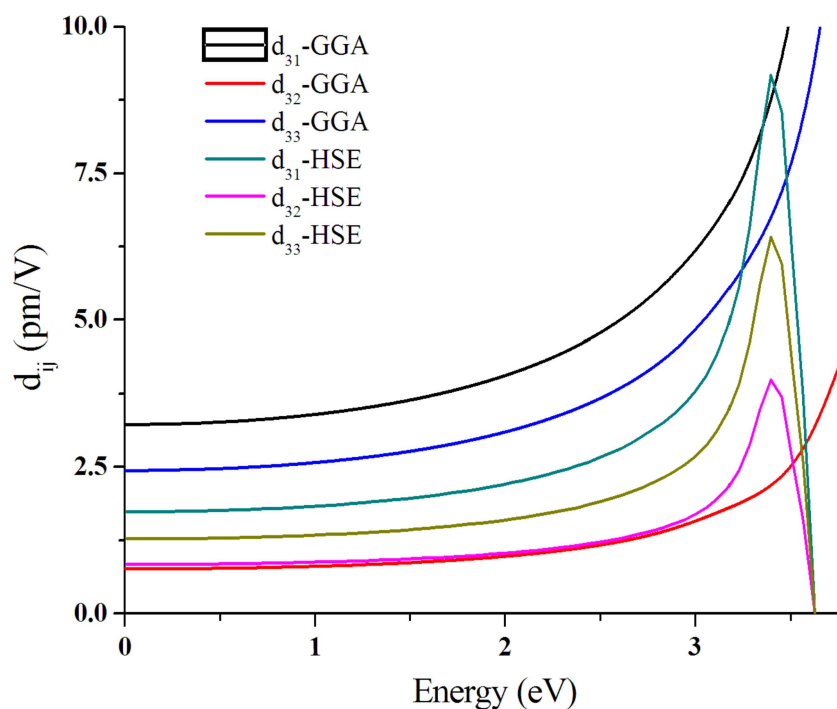


Figure 6. Calculated frequency-dependent second harmonic generation coefficients for $\text{Rb}_2\text{Na}(\text{NO}_3)_3$ by generalized gradient approximation (GGA) and Heyd–Scuseria–Ernzerhof (HSE) functionals.

3. Materials and Methods

3.1. Materials and Synthesis

Single crystals of $\text{Rb}_2\text{Na}(\text{NO}_3)_3$ were grown through solid state reactions. A mixture of RbNO_3 (Alfa Aesar, 99%), (Alfa Aesar, Seoul, Korea), NaNO_3 (Alfa Aesar, 99%), and NH_4NO_3 (Alfa Aesar, 99%) in a molar ratio of 4:2:1 was thoroughly ground in a mortar and pestle and transferred into a platinum crucible. The reaction mixture was heated at 300 °C for one day until a transparent melt was formed. The melt was allowed to cool slowly at a rate of 3 °C/h to the final crystallization temperature, 150 °C. After that the obtained product mixture was quenched to room temperature. Colorless transparent crystals shown in Figure S3 in the Supplementary Materials were obtained. Pure polycrystalline samples of $\text{Rb}_2\text{Na}(\text{NO}_3)_3$ were synthesized through the solid state reactions from the stoichiometric mixture of RbNO_3 and NaNO_3 at 150 °C for 2 days. Synthesized $\text{Rb}_2\text{Na}(\text{NO}_3)_3$ has been deposited to the Noncentrosymmetric Materials Bank <http://ncsmb.knrrc.or.kr>.

3.2. Single Crystal Structure Determination

Single crystal X-ray diffraction data of $\text{Rb}_2\text{Na}(\text{NO}_3)_3$ were collected at room temperature on a Bruker SMART BREEZE diffractometer (Bruker, Karlsruhe, Germany) equipped with a 1K CCD area detector using graphite monochromated Mo $K\alpha$ radiation. The structure was solved by the direct method and refined by full-matrix least-squares fitting on F^2 using SHELX-97 [61]. The refined structure was verified using the ADDSYM algorithm from the program PLATON [62], and no higher symmetries were found. CCDC 1449459 contains the supplementary crystallographic data for this paper. These data can be obtained free of charge via <http://www.ccdc.cam.ac.uk/conts/retrieving.html> (or from the CCDC, 12 Union Road, Cambridge CB2 1EZ, UK; Fax: +44-1223-336033; E-mail: deposit@ccdc.cam.ac.uk). Relevant crystallographic data and details of the experimental conditions for $\text{Rb}_2\text{Na}(\text{NO}_3)_3$ are summarized in Table 2. Atomic coordinates and isotropic displacement parameters are listed in Table 3. Selected bond lengths and angles for $\text{Rb}_2\text{Na}(\text{NO}_3)_3$ are listed in Table S1 in the Supplementary Materials.

Table 2. Crystallographic Data for Rb₂Na(NO₃)₃.

CCDC NO	1449459
formula	Rb ₂ Na(NO ₃) ₃
fw	379.96
crystal system	Orthorhombic
space group	<i>Pmc</i> 2 ₁ (No. 26)
<i>a</i> (Å)	5.313(2)
<i>b</i> (Å)	9.077(4)
<i>c</i> (Å)	9.700(4)
<i>V</i> (Å ³)	467.8(4)
<i>Z</i>	2
ρ_{calcd} (g/cm ³)	2.697
<i>T</i> (K)	298.0(2)
λ (Å)	0.71073
<i>R</i> (<i>F</i>) ^a	0.029
<i>R</i> _w (<i>F</i> _o ²) ^b	0.069
Flack parameter	0.017(16)

$$^a R(F) = \frac{\sum ||F_o| - |F_c||}{\sum |F_o|}. \quad ^b R_w(F_o^2) = [\sum w(F_o^2 - F_c^2)^2 / \sum w(F_o^2)^2]^{1/2}.$$

Table 3. Atomic Coordinates, Isotropic Displacement Parameters, and Bond Valence Sums for Rb₂Na(NO₃)₃.

	<i>x</i>	<i>y</i>	<i>z</i>	<i>U</i> _{eq} ^a	BVS
Rb(1)	0.5	0.08284 (7)	0.53258 (6)	0.0278 (2)	1.22
Rb(2)	0.5	−0.37843 (7)	0.70652 (6)	0.0290 (2)	1.14
Na(1)	1	0.2987 (3)	0.7520 (3)	0.0312 (6)	1.13
N(1)	1	−0.0531 (6)	0.7396 (6)	0.0238 (11)	5.04
N(2)	0.5	−0.2517 (6)	0.3837 (6)	0.0249 (11)	4.94
N(3)	1	0.4120 (6)	0.4519 (6)	0.0234 (12)	5.03
O(1)	1	0.0592 (6)	0.6636 (6)	0.0365 (12)	2.11
O(2)	0.7910 (10)	−0.1055 (5)	0.7734 (6)	0.0557 (12)	2.08
O(3)	0.2975 (7)	−0.2289 (4)	0.4447 (4)	0.0394 (9)	2.01
O(4)	0.5	−0.2987 (6)	0.2620 (5)	0.0343 (11)	2.09
O(5)	1	0.5419 (6)	0.8311 (6)	0.0340 (11)	2.13
O(6)	0.7977 (10)	0.3903 (5)	0.5120 (6)	0.0573 (12)	1.97

^a *U*_{eq} is defined as one third of the trace of the orthogonalized *U*_{ij} tensor.

3.3. Powder X-Ray Diffraction (PXRD)

The PXRD data were obtained on a Bruker D8-Advance diffractometer (Bruker, Karlsruhe, Germany) using Cu K α radiation at room temperature with 40 kV and 40 mA in the 2 θ range of 5–70° with a scan step width of 0.05° and a fixed time of 0.2 s. The PXRD pattern for Rb₂Na(NO₃)₃ showed a very good agreement with the calculated data from the single-crystal model.

3.4. Thermal Analysis

The thermogravimetric/differential thermal analysis (TG/DTA) scans were performed on a NETZSCH STA 449C simultaneous analyzer (NETZSCH, Bavaria, Germany). The reference (Al₂O₃) and polycrystalline Rb₂Na(NO₃)₃ were enclosed in separate alumina crucibles and heated from room temperature to 500 °C at a rate of 10 °C/min under a constant flow of nitrogen gas. The TG residues

were visually inspected and then analyzed by powder X-ray diffraction (Bruker, Karlsruhe, Germany) after heating.

3.5. Infrared (IR) Spectroscopy

IR spectrum of the sample was recorded on a Thermo Scientific Nicolet 6700 FT-IR spectrometer (Thermo Electron Corporation, Waltham, MA, USA) in the 400–4000 cm^{-1} range, with the sample embedded in a KBr matrix.

3.6. UV-Vis Diffuse Reflectance Spectroscopy

UV-Vis diffuse reflectance spectral data were obtained on a Varian Cary 500 scan UV-Vis-NIR spectrophotometer (Varian, Palo Alto, CA, USA) over the spectral range 200–2500 nm at room temperature. The reflectance spectrum was transformed into the absorbance data using the Kubelka–Munk function [50,51].

3.7. Scanning Electron Microscope (SEM)/Energy-Dispersive Analysis by X-ray (EDX)

SEM/EDX analyses have been performed using a Hitachi S-3400N/Horiba Energy EX-250 instruments (Hitachi, Tokyo, Japan). EDX for $\text{Rb}_2\text{Na}(\text{NO}_3)_3$ reveals an approximate Rb:Na ratio of 2.1:1.0.

3.8. Second-Harmonic Generation (SHG) Measurements

Powder SHG measurements were performed using a modified Kurtz and Perry NLO measurement system (Jinsung, Daejeon, Korea) with 1064 nm radiation [52]. A more detailed explanation of the methods and the apparatus utilized has been published previously [2].

3.9. Computational Details

The density functional theory (DFT) calculations for the experimental crystal structure of $\text{Rb}_2\text{Na}(\text{NO}_3)_3$ were carried out using the CASTEP code [63]. The generalized gradient approximation (GGA) of Perdew–Burke–Ernzerhof (PBE) [64] and the hybrid functional HSE06 [65] were chosen. The converge criteria of energy was 10^{-5} eV/atom. The cutoff energy for the plane wave basis was set to be 850 eV. The k -points sampling in the Brillouin zone was placed to be $3 \times 3 \times 4$ according to the Monkhorst–Pack scheme [66]. The valences of composed atoms were as follows: Rb $4s^2 4p^6 5s^1$; Na $2s^2 2p^6 3s^1$; N $2s^2 2p^3$; O $2s^2 2p^4$. The calculated second-order susceptibilities are indicated in terms of the first-order susceptibilities as follows:

$$\chi_{ijk}^{(2)}(-\omega_3; \omega_1, \omega_2) = F^{(2)} \chi_{ii}^{(1)}(\omega_3) \chi_{jj}^{(1)}(\omega_1) \chi_{kk}^{(1)}(\omega_2) \quad (5)$$

This was obtained from a classical anharmonic oscillator (AHO) model [67], in which $F^{(2)}$ is local field correction and is defined as:

$$F^{(2)} = \frac{m \varepsilon_0^2 \omega_0^2}{N^2 e^3 d} \quad (6)$$

where d is the lattice constant, e is the electron charge, N is the atomic density, ω_0 is the atomic resonance frequency, ε_0 is the permittivity of free space, and m is the electron mass. The first-order susceptibility at the low-frequency region is given by $\chi_{ii}^{(1)}(\omega) = [\varepsilon(\omega)_i - 1]/4\pi$, and the dielectric function $\varepsilon(\omega)_i$ are obtained from the optical properties calculation of CASTEP.

4. Conclusions

A NCS mixed alkali metal nitrate NLO material, $\text{Rb}_2\text{Na}(\text{NO}_3)_3$, has been synthesized through conventional solid state reactions. The material features an anionic layered structure. Powder SHG measurements reveal that $\text{Rb}_2\text{Na}(\text{NO}_3)_3$ is phase-matchable (type I) with a very large SHG response of

approximately five times that of KDP. The strong SHG efficiency of the material is attributed to the high density and the optimized arrangement of the NLO-active NO₃ groups in the structure, which is in good agreement with the results obtained from the theoretical calculations. In addition, Rb₂Na(NO₃)₃ exhibits a wide transparent region ranging from UV to near IR and melts congruently. On the basis of these arguments, this compound is a potential candidate for applications in novel UV-NLO materials. Our future research efforts will be devoted to growing large crystals of Rb₂Na(NO₃)₃ to further study their optical properties, such as refractive indices, the Sellmeier equations, second-order NLO coefficients, and laser damage threshold.

Supplementary Materials: The following are available online at <http://www.mdpi.com/2073-4352/6/4/42/s1>. Table S1: Selected Bond lengths (Å) and angles (deg) for Rb₂Na(NO₃)₃; Figure S1: Crystal structure of Sr₂(OH)₃NO₃ (a) and K₂La(NO₃)₅·2H₂O (b); Figure S2: Calculated band structure of Rb₂Na(NO₃)₃ (the Fermi level is set at 0 eV); Figure S3: Photograph of Rb₂Na(NO₃)₃ crystal.

Acknowledgments: This research was supported by the National Research Foundation of Korea (NRF) funded by the Korea government (No. 2014M3A9B8023478). Guohong Zou and Chensheng Lin thank the National Natural Science Foundation of China (NOs. 21401178 and 21501161).

Author Contributions: Guohong Zou conceived and designed this study, carried out experimental work (synthesis, crystallization and characterization) and wrote the manuscript. Chensheng Lin carried out the calculation and analysis. Hyung Gu Kim and Hongil Jo contributed reagents/materials/analysis tools. Kang Min Ok conceived and coordinated the project.

Conflicts of Interest: The authors declare no conflict of interest.

References

1. Nguyen, S.D.; Yeon, J.; Kim, S.H.; Halasyamani, P.S. BiO(IO₃): A new polar iodate that exhibits an aurivillius-type (Bi₂O₂)⁽²⁺⁾ layer and a large SHG response. *J. Am. Chem. Soc.* **2011**, *133*, 12422–12425. [[CrossRef](#)] [[PubMed](#)]
2. Ok, K.M.; Chi, E.O.; Halasyamani, P.S. Bulk characterization methods for non-centrosymmetric materials: second-harmonic generation, piezoelectricity, pyroelectricity, and ferroelectricity. *Chem. Soc. Rev.* **2006**, *35*, 710–717. [[CrossRef](#)] [[PubMed](#)]
3. Ok, K.M.; Halasyamani, P.S. The lone-pair cation I⁵⁺ in a hexagonal tungsten oxide-like framework: Synthesis, structure, and second-harmonic generating properties of Cs₂I₄O₁₁. *Angew. Chem. Int. Ed.* **2004**, *43*, 5489–5491. [[CrossRef](#)] [[PubMed](#)]
4. Song, J.L.; Hu, C.L.; Xu, X.; Kong, F.; Mao, J.G. A facile synthetic route to a new SHG material with two types of parallel pi-conjugated planar triangular units. *Angew. Chem. Int. Ed.* **2015**, *54*, 3679–3682. [[CrossRef](#)] [[PubMed](#)]
5. Sun, C.F.; Hu, C.L.; Xu, X.; Yang, B.P.; Mao, J.G. Explorations of new second-order nonlinear optical materials in the potassium vanadyl iodate system. *J. Am. Chem. Soc.* **2011**, *133*, 5561–5572. [[CrossRef](#)] [[PubMed](#)]
6. Yang, B.P.; Hu, C.L.; Xu, X.; Sun, C.F.; Zhang, J.H.; Mao, J.G. NaVO₂(IO₃)₂(H₂O): A unique layered material produces a very strong SHG response. *Chem. Mater.* **2010**, *22*, 1545–1550. [[CrossRef](#)]
7. Yu, H.W.; Wu, H.P.; Pan, S.; Yang, Z.H.; Hou, X.L.; Su, X.; Jing, Q.; Poeppelmeier, K.R.; Rondinelli, J.M. Cs₃Zn₆B₉O₂₁: A chemically benign member of the KBBF family exhibiting the largest second harmonic generation response. *J. Am. Chem. Soc.* **2014**, *136*, 1264–1267. [[CrossRef](#)] [[PubMed](#)]
8. Wu, H.P.; Yu, H.W.; Yang, Z.H.; Hou, X.L.; Su, X.; Pan, S.L.; Poeppelmeier, K.R.; Rondinelli, J.M. Designing a deep-ultraviolet nonlinear optical material with a large second harmonic generation response. *J. Am. Chem. Soc.* **2013**, *135*, 4215–4218. [[CrossRef](#)] [[PubMed](#)]
9. Yang, Y.; Pan, S.L.; Li, H.Y.; Han, J.A.; Chen, Z.H.; Zhao, W.W.; Zhou, Z.D. Li₄Cs₃B₇O₁₄: Synthesis, crystal structure, and optical properties. *Inorg. Chem.* **2011**, *50*, 2415–2419. [[CrossRef](#)] [[PubMed](#)]
10. Zou, G.H.; Ma, Z.J.; Wu, K.C.; Ye, N. Cadmium-rare earth oxyborates Cd₄ReO(BO₃)₃ (Re = Y, Gd, Lu): Congruently melting compounds with large SHG responses. *J. Mater. Chem.* **2012**, *22*, 19911–19918. [[CrossRef](#)]
11. Wang, S.C.; Ye, N. Na₂CsBe₆B₅O₁₅: An alkaline beryllium borate as a Deep-UV nonlinear optical crystal. *J. Am. Chem. Soc.* **2011**, *133*, 11458–11461. [[CrossRef](#)] [[PubMed](#)]

12. Wang, S.C.; Ye, N.; Li, W.; Zhao, D. Alkaline beryllium borate NaBeB_3O_6 and $\text{ABe}_{(2)}\text{B}_{(3)}\text{O}_{(7)}$ ($A = \text{K, Rb}$) as UV nonlinear optical crystals. *J. Am. Chem. Soc.* **2010**, *132*, 8779–8786. [[CrossRef](#)] [[PubMed](#)]
13. Li, R.K.; Chen, P. Cation coordination control of anionic group alignment to maximize SHG effects in the BaMBO_3F ($M = \text{Zn, Mg}$) series. *Inorg. Chem.* **2010**, *49*, 1561–1565. [[CrossRef](#)] [[PubMed](#)]
14. Zhou, T.H.; Wang, D.P.; Goh, S.C.K.; Hong, J.D.; Han, J.Y.; Mao, J.G.; Xu, R. Bio-inspired organic cobalt(II) phosphonates toward water oxidation. *Energy Environ. Sci.* **2015**, *8*, 526–534. [[CrossRef](#)]
15. Becker, P. Borate materials in nonlinear optics. *Adv. Mater.* **1998**, *10*, 979–992. [[CrossRef](#)]
16. Chen, C.T.; Wu, B.C.; Jiang, A.D. A new-type ultraviolet SHG crystal-Beta- BaB_2O_4 . *Sci. Sin. Ser. B* **1985**, *28*, 235–243.
17. Chen, C.; Wu, Y.; Jiang, A.; Wu, B.; You, G.; Li, R.; Lin, S. New nonlinear-optical crystal: LiB_3O_5 . *J. Opt. Soc. Am. B* **1989**, *6*, 616–621. [[CrossRef](#)]
18. Wu, Y.; Sasaki, T.; Nakai, S.; Yokotani, A.; Tang, H.; Chen, C. CsB_3O_5 : A new nonlinear optical crystal. *Appl. Phys. Lett.* **1993**, *62*, 2614–2615. [[CrossRef](#)]
19. Mori, Y.; Kuroda, I.; Nakajima, S.; Sasaki, T.; Nakai, S. New nonlinear optical crystal: Cesium lithium borate. *Appl. Phys. Lett.* **1995**, *67*, 1818–1820. [[CrossRef](#)]
20. Tu, J.-M.; Keszler, D.A. $\text{CsLiB}_6\text{O}_{10}$: A noncentrosymmetric polyborate. *Mater. Res. Bull.* **1995**, *30*, 209–215. [[CrossRef](#)]
21. Mei, L.; Wang, Y.; Chen, C.; Wu, B. Nonlinear optical materials based on $\text{MBe}_2\text{BO}_3\text{F}_2$ ($M = \text{Na, K}$). *J. Appl. Phys.* **1993**, *74*, 7014–7015. [[CrossRef](#)]
22. Chen, C.; Wang, Y.; Wu, B.; Wu, K.; Zeng, W.; Yu, L. Design and synthesis of an ultraviolet-transparent nonlinear optical crystal $\text{Sr}_2\text{Be}_2\text{B}_2\text{O}_7$. *Nature* **1995**, *373*, 322–324. [[CrossRef](#)]
23. Chen, C. Localized quantal theoretical treatment, based on an anionic coordination polyhedron model, for the EO and SHG effects in crystals of the mixed-oxide types. *Sci. Sin.* **1979**, *22*, 756–776.
24. Chen, C.; Liu, G.-Z. Recent advances in nonlinear optical and electro-optical materials. *Annu. Rev. Mater. Sci.* **1986**, *16*, 203–243. [[CrossRef](#)]
25. Chen, C.; Wu, Y.; Li, R. The anionic group theory of the non-linear optical effect and its applications in the development of new high-quality NLO crystals in the borate series. *Int. Rev. Phys. Chem.* **1989**, *8*, 65–91. [[CrossRef](#)]
26. Luo, M.; Lin, C.S.; Zou, G.H.; Ye, N.; Cheng, W.D. Sodium-rare earth carbonates with shorite structure and large second harmonic generation response. *CrystEngComm* **2014**, *16*, 4414–4421. [[CrossRef](#)]
27. Luo, M.; Ye, N.; Zou, G.H.; Lin, C.S.; Cheng, W.D. $\text{Na}_8\text{Lu}_2(\text{CO}_3)_6\text{F}_2$ and $\text{Na}_3\text{Lu}(\text{CO}_3)_2\text{F}_2$: Rare earth fluoride Carbonates as deep-UV nonlinear optical materials. *Chem. Mater.* **2013**, *25*, 3147–3153. [[CrossRef](#)]
28. Zou, G.H.; Huang, L.; Ye, N.; Lin, C.S.; Cheng, W.D.; Huang, H. CsPbCO_3F : A strong second-harmonic generation material derived from enhancement via p-pi interaction. *J. Am. Chem. Soc.* **2013**, *135*, 18560–18566. [[CrossRef](#)] [[PubMed](#)]
29. Zou, G.H.; Ye, N.; Huang, L.; Lin, X.S. Alkaline-alkaline earth fluoride carbonate crystals $\text{ABCO}_{(3)}\text{F}$ ($A = \text{K, Rb, Cs}$; $B = \text{Ca, Sr, Ba}$) as nonlinear optical materials. *J. Am. Chem. Soc.* **2011**, *133*, 20001–20007. [[CrossRef](#)] [[PubMed](#)]
30. Luo, M.; Wang, G.X.; Lin, C.S.; Ye, N.; Zhou, Y.Q.; Cheng, W.D. $\text{Na}_4\text{La}_2(\text{CO}_3)_5$ and $\text{CsNa}_5\text{Ca}_5(\text{CO}_3)_8$: Two new carbonates as UV nonlinear optical materials. *Inorg. Chem.* **2014**, *53*, 8098–8104. [[CrossRef](#)] [[PubMed](#)]
31. Tran, T.T.; He, J.G.; Rondinelli, J.M.; Halasyamani, P.S. RbMgCO_3F : A new beryllium-free deep-ultraviolet nonlinear optical material. *J. Am. Chem. Soc.* **2015**, *137*, 10504–10507. [[CrossRef](#)] [[PubMed](#)]
32. Tran, T.T.; Halasyamani, P.S.; Rondinelli, J.M. Role of acentric displacements on the crystal structure and second-harmonic generating properties of RbPbCO_3F and CsPbCO_3F . *Inorg. Chem.* **2014**, *53*, 6241–6251. [[CrossRef](#)] [[PubMed](#)]
33. Tran, T.T.; Halasyamani, P.S. New fluoride carbonates: Centrosymmetric $\text{KPb}_2(\text{CO}_3)_2\text{F}$ and noncentrosymmetric $\text{K}_{2.70}\text{Pb}_{5.15}(\text{CO}_3)_5\text{F}_3$. *Inorg. Chem.* **2013**, *52*, 2466–2473. [[CrossRef](#)] [[PubMed](#)]
34. Chang, L.X.; Wang, L.; Su, X.; Pan, S.; Hailili, R.; Yu, H.W.; Yang, Z.H. A nitrate nonlinear optical crystal $\text{Pb}_{16}(\text{OH})_{(16)}(\text{NO}_3)_{(16)}$ with a large second-harmonic generation response. *Inorg. Chem.* **2014**, *53*, 3320–3325. [[CrossRef](#)] [[PubMed](#)]
35. Wang, G.; Luo, M.; Ye, N.; Lin, C.; Cheng, W. Series of lead oxide hydroxide nitrates obtained by adjusting the pH values of the reaction systems. *Inorg. Chem.* **2014**, *53*, 5222–5228. [[CrossRef](#)] [[PubMed](#)]

36. Wang, G.; Luo, M.; Lin, C.; Ye, N.; Zhou, Y.; Cheng, W. Lanthanum lead oxide hydroxide nitrates with a nonlinear optical effect. *Inorg. Chem.* **2014**, *53*, 12584–12589. [[CrossRef](#)] [[PubMed](#)]
37. Huang, L.; Zou, G.H.; Cai, H.Q.; Wang, S.C.; Lin, C.S.; Ye, N. Sr₂(OH)₃NO₃: The first nitrate as a deep UV nonlinear optical material with large SHG responses. *J. Mater. Chem. C* **2015**, *3*, 5268–5274. [[CrossRef](#)]
38. Li, R.K. *Exploration Research on Inorganic UV Nonlinear Optical Crystal*; Fujian Institute of Research on the Structure of Matter: Fuzhou, China, 1988.
39. Chi, E.O.; Ok, K.M.; Porter, Y.; Halasyamani, P.S. Na₂Te₃Mo₃O₁₆: A new molybdenum tellurite with second-harmonic generating and pyroelectric properties. *Chem. Mater.* **2006**, *18*, 2070–2074. [[CrossRef](#)]
40. Ra, H.-S.; Ok, K.M.; Halasyamani, P.S. Combining second-order Jahn-Teller distorted cations to create highly efficient SHG materials: Synthesis, characterization, and NLO properties of BaTeM₂O₉ (M = Mo⁶⁺ or W⁶⁺). *J. Am. Chem. Soc.* **2003**, *125*, 7764–7765. [[CrossRef](#)] [[PubMed](#)]
41. Sykora, R.E.; Ok, K.M.; Halasyamani, P.S.; Albrecht-Schmitt, T.E. Structural modulation of molybdenyl iodate architectures by alkali metal cations in AMoO₃ (IO₃) (A = K, Rb, Cs): A facile route to new polar materials with large SHG responses. *J. Am. Chem. Soc.* **2002**, *124*, 1951–1957. [[CrossRef](#)] [[PubMed](#)]
42. Zhang, W.-L.; Cheng, W.-D.; Zhang, H.; Geng, L.; Lin, C.-S.; He, Z.-Z. A strong second-harmonic generation material Cd₄BiO(BO₃)₃ originating from 3-chromophore asymmetric structures. *J. Am. Chem. Soc.* **2010**, *132*, 1508–1509. [[CrossRef](#)] [[PubMed](#)]
43. Inaguma, Y.; Yoshida, M.; Katsumata, T. A polar oxide ZnSnO₃ with a LiNbO₃-type structure. *J. Am. Chem. Soc.* **2008**, *130*, 6704–6705. [[CrossRef](#)] [[PubMed](#)]
44. Phanon, D.; Gautier-Luneau, I. Promising material for infrared nonlinear optics: NaI₃O₈ salt containing an Octaoxotriiodate (V) anion formed from condensation of [IO₃][−] ions. *Angew. Chem. Int. Ed.* **2007**, *46*, 8488–8491. [[CrossRef](#)] [[PubMed](#)]
45. Huang, Y.-Z.; Wu, L.-M.; Wu, X.-T.; Li, L.-H.; Chen, L.; Zhang, Y.-F. Pb₂B₅O₉I: An iodide borate with strong second harmonic generation. *J. Am. Chem. Soc.* **2010**, *132*, 12788–12789. [[CrossRef](#)] [[PubMed](#)]
46. Sun, C.-F.; Hu, C.-L.; Xu, X.; Ling, J.-B.; Hu, T.; Kong, F.; Long, X.-F.; Mao, J.-G. BaNbO (IO₃)₅: A new polar material with a very large SHG response. *J. Am. Chem. Soc.* **2009**, *131*, 9486–9487. [[CrossRef](#)] [[PubMed](#)]
47. Ksiksi, N.; Driss, M.; Hellali, D.; Guesmi, A.; Zamali, H. Le nitrate double NaRb₂(NO₃)₃, composé intermédiaire du système binaire isobare NaNO₃-RbNO₃: Études thermiques et cristallographiques. *Acta Crystallogr.* **2015**, *71*, 455–458. [[CrossRef](#)] [[PubMed](#)]
48. Brese, N.E.; O'Keeffe, M. Bond-valence parameters for solids. *Acta Crystallogr.* **1991**, *47*, 192–197. [[CrossRef](#)]
49. Brown, I.D.; Altermatt, D. Bond-valence parameters obtained from a systematic analysis of the inorganic crystal structure database. *Acta Crystallogr.* **1985**, *41*, 244–247. [[CrossRef](#)]
50. Tauc, J. Absorption edge and internal electric fields in amorphous semiconductors. *Mater. Res. Bull.* **1970**, *5*, 721–729. [[CrossRef](#)]
51. Kubelka, P. Ein Beitrag zur optik der farban striche. *Z. Tech. Phys.* **1931**, *12*, 593–603.
52. Kurtz, S.; Perry, T. A powder technique for the evaluation of nonlinear optical materials. *J. Appl. Phys.* **1968**, *39*, 3798–3813. [[CrossRef](#)]
53. Eckardt, R.C.; Masuda, H.; Fan, Y.X.; Byer, R.L. Absolute and relative nonlinear optical coefficients of KDP, BaB₂O₄, LiIO₃, MgO: LiNbO₃, and KTP measured by phase-matched second-harmonic generation. *IEEE J. Quantum Electron.* **1990**, *26*, 922–933. [[CrossRef](#)]
54. Ye, N.; Chen, Q.; Wu, B.; Chen, C. Searching for new nonlinear optical materials on the basis of the anionic group theory. *J. Appl. Phys.* **1998**, *84*, 555–558. [[CrossRef](#)]
55. Xue, D.; Zhang, S. Calculation of nonlinearities of K₂Ce(NO₃)₅ · 2H₂O and K₂La(NO₃)₅ · 2H₂O. *Mol. Phys.* **1998**, *93*, 411–415. [[CrossRef](#)]
56. Godby, R.W.; Schlüter, M.; Sham, L.J. Trends in self-energy operators and their corresponding exchange-correlation potentials. *Phys. Rev. B* **1987**, *36*, 6497–6500. [[CrossRef](#)]
57. Okoye, C. Theoretical study of the electronic structure, chemical bonding and optical properties of KNbO₃ in the paraelectric cubic phase. *J. Phys. Condens. Matter* **2003**, *15*, 5945. [[CrossRef](#)]
58. Terki, R.; Bertrand, G.; Aourag, H. Full potential investigations of structural and electronic properties of ZrSiO₄. *Microelectron. Eng.* **2005**, *81*, 514–523. [[CrossRef](#)]
59. Seidler, T.; Stadnicka, K.; Champagne, B. Linear and second-order nonlinear optical properties of ionic organic crystals. *J. Chem. Phys.* **2014**, *141*, 104109. [[CrossRef](#)] [[PubMed](#)]

60. Lacivita, V.; Rérat, M.; Kirtman, B.; Ferrero, M.; Orlando, R.; Dovesi, R. Calculation of the dielectric constant ϵ and first nonlinear susceptibility $\chi^{(2)}$ of crystalline potassium dihydrogen phosphate by the coupled perturbed Hartree–Fock and coupled perturbed Kohn–Sham schemes as implemented in the crystal code. *J. Chem. Phys.* **2009**, *131*, 204509. [[CrossRef](#)] [[PubMed](#)]
61. Sheldrick, G.M. A short history of SHELX. *Acta Crystallogr.* **2007**, *64*, 112–122. [[CrossRef](#)] [[PubMed](#)]
62. Spek, A.L. Single-crystal structure validation with the program PLATON. *J. Appl. Crystallogr.* **2003**, *36*, 7–13. [[CrossRef](#)]
63. Segall, M.D.; Lindan, P.J.D.; Probert, M.J.; Pickard, C.J.; Hasnip, P.J.; Clark, S.J.; Payne, M.C. First-principles simulation: Ideas, illustrations and the CASTEP code. *J. Phys. Condens. Matter* **2002**, *14*, 2717–2744. [[CrossRef](#)]
64. Perdew, J.P.; Burke, K.; Ernzerhof, M. Generalized gradient approximation made simple. *Phys. Rev. Lett.* **1996**, *77*, 3865–3868. [[CrossRef](#)] [[PubMed](#)]
65. Heyd, J.; Scuseria, G.E.; Ernzerhof, M. Hybrid functionals based on a screen Coulomb potential. *J. Chem. Phys.* **2003**, *118*, 8207–8215. [[CrossRef](#)]
66. Monkhorst, H.J.; Pack, J.D. Special points for Brillouin-zone integrations. *Phys. Rev. B* **1976**, *13*, 5188–5192. [[CrossRef](#)]
67. Boyd, R.W. *Nonlinear Optics*; Academic Press: New York, NY, USA, 1992; pp. 21–47.



© 2016 by the authors; licensee MDPI, Basel, Switzerland. This article is an open access article distributed under the terms and conditions of the Creative Commons Attribution (CC-BY) license (<http://creativecommons.org/licenses/by/4.0/>).